Journal of Cluster Science (2020) 31:277–286
https://doi.org/10.1007/s10876-019-01645-1

ORIGINAL PAPER

Fabrication of Ultrathin Nanosheets of Graphitic Carbon Nitride Heterojunction with Spherical Shaped Bi_2O_3 Nanoparticles for High Performance Visible Light Photocatalyst

M. Sumathi[1] · A. Prakasam[1] · P. M. Anbarasan[2]

Received: 6 June 2019 / Published online: 27 July 2019

Abstract
A combined microwave-calcinations approach is developed to synthesize of β-Bi_2O_3/g-C_3N_4 hybrid nanocomposite and methodically investigated their structural, optical and photocatalytic properties. XRD and TEM results divulge that tetragonal structure and the individual spherical shaped nanoparticles 35–40 nm were uniformly scattered over the g-C_3N_4 sheets. The formation of g-C_3N_4 and β-Bi_2O_3 can develop the light absorption ability and separation of photogenerated carriers of β-Bi_2O_3, which is confirmed through photoluminescence and UV–Vis DRS analysis. The photocatalytic degradation of congo-red (CR) and malachite green (MG) dyes were evaluated under visible light irradiation. The β-Bi_2O_3/g-C_3N_4 heterojunction exhibited higher photocatalytic activity towards MG dye such as high photodegradation efficiency (94.8%) and good stability (92%) than bare β-Bi_2O_3. This could be due to the high surface area and synergic effect between the β-Bi_2O_3 and g-C_3N_4 p–n junctions. This work provides an efficient β-Bi_2O_3/g-C_3N_4 hybrid for removal of toxic pollutants and waste water treatments.

Keywords β-Bi_2O_3/g-C_3N_4 · Microwave irradiation · Surface plasmonic resonance · Photocatalyst · Visible light

Introduction

As a drawback of financial advancement within the last decades, progressively more serious pollution of the environment has raised much concern over potential dangers to the ecosystem and human wellbeing [1–3]. Colossal endeavors have been committed to the decrease of environmental contaminants, and photocatalysis-based procedures have developed as a promising pathway for natural purification [4–7]. As a conceivable arrangement to the issues of developing worldwide energy needs and environmental contamination, photocatalysis has drawn huge consideration due to its potential application in natural pollutants disposal, water splitting and dye-sensitized solar cells [8–16]. Recently, various types of semiconducting metal oxides (ZnO, WO_3, SnO_2, TiO_2 etc.) have been broadly studied as photocatalyst materials. Among these, bismuth oxide (Bi_2O_3) has been most valuable photocatalyst, which showed high photocatalytic performance for toxin degradation in wastewater under ultraviolet and visible light illumination [17–20]. Moreover, Bi_2O_3 has been extensively studied as photocatalytic material because of its high absorption properties of both UV and visible light and suitable band gap (ca. 2.31 eV). Nevertheless, as a visible-light photocatalyst, bare Bi_2O_3 has a poor degradation efficiency of organic pollutants for its slight absorption rate of incident photons and very low separation rate of photogene rated electron–hole pairs [21]. Hence, growing composite based hybrid photocatalysts with high visible light response, fast photogenerated carrier separation efficiency and good stability were considered as an effective way for enhancement of photocatalytic activity.

It is well known that graphitic carbon nitrite (g-C_3N_4) is an organic semiconductor, displays capable photocatalytic behavior towards numerous organic pollutants under visible light illumination. It has achieved plenty of

✉ A. Prakasam
aptgac@gmail.com

[1] PG and Research Department of Physics, Thiruvalluvar Government Arts College, Rasipuram, Tamilnadu 637401, India

[2] Nano and Hybrid Materials Laboratory, Department of Physics, Periyar University, Salem, Tamilnadu 636011, India

consideration because of its outstanding chemical stability, adsorption ability, and suitable band gap of 2.7 eV [22]. In addition, the combinations of g-C_3N_4/metal oxides will reduce the band gap and increasing the photogenerated carrier separation efficiency, which enhancing the photocatalytic efficiency of hybrid photocatalyst. Hence, we report on the combination of metal free g-C_3N_4/β-Bi_2O_3 hybrid photocatalyst by using simple microwave irradiation method for the first time. The loading of different g-C_3N_4 on the β-Bi_2O_3 has been systematically investigated through structural, optical and photocatalytic properties. The β-Bi_2O_3/g-C_3N_4 heterojunction exhibited higher photocatalytic activity towards MG dye such as high photodegradation efficiency (94.8%) and good stability (92%) than bare β-Bi_2O_3. This could be due to the high surface area and synergic effect between the β-Bi_2O_3 and g-C_3N_4 p–n junctions. Moreover, this method is simple, cost effective and less time consuming (about 10 min), and for large-scale production [23].

Materials and Methods

Materials

Bismuth nitrate pentahydrate ($Bi(NO_3)_3{\cdot}5H_2O$) and Urea (CN_2H_4O) was purchased from Sigma-Aldrich were used as gotten without advance refinement.

Preparation of g-C_3N_4

Graphitic carbon nitride (g-C_3N_4) was synthesized by pyrolysis of urea in a muffle furnace; 10 g urea was put into an alumina crucible with a cover, and then heated to 400 °C for 2 h in air atmosphere. The heating rate of the whole reaction was 1 °C min^{-1}. The yellow power (g-C_3N_4) was collected. The received amount of the g-C_3N_4 was about 2 g.

Preparation of Bi_2O_3 and Bi_2O_3/g-C_3N_4 Composites

In the typical synthesis of Bi_2O_3, 1 mmol of bismuth nitrate pentahydrate and 4 mmol of urea were mixed with 50 mL of DI under strong magnetic stirring. The resulting solution was transferred into a Teflon-lined household microwave oven (2.45 GHz) and irradiated for 10 min at 900 W of microwave power. Then obtained precipitate was collected by centrifugation, washed several times with DI water and absolute ethanol successively, and then was dried at 50 °C in an oven in air atmosphere. Finally the light brown color Bi_2O_3 nanopowder was obtained. The synthesis of the Bi_2O_3/g-C3N4 composite was as follows: Bi_2O_3 and g-C3N4 at a specific mass ratio (25, 50 and 100 mg) were mixed and ground for 3 min using a mortar and pestle. The mixed powder was placed in an alumina crucible with a cover and heated at 400 °C in a muffle furnace for 4 h. The ratio of Bi_2O_3 and g-C_3N_4 is 1:0.5, 1:1 and 1:1.5. The final products were named as BO, BG1, BG2 and BG3 for adding 0, 25, 50 and 100 mg of g-C_3N_4.

Characterization Techniques

The crystalline structures and compositions of the products were gained using powder X-ray diffraction (PXRD, Bruker D8 Progress) utilizing Cu-K_λ as the radiation source (wavelength: 1.54056 Å) and the scanning speed of 2 °C min^{-1}. The morphology of the samples was performed by a JEOL JEM 2100F high-resolution transmission electronic magnifying instrument (HRTEM). DRS measurements were carried out employing a Hitachi UV-365 spectrophotometer prepared with a coordination circle connection with the wavelength ranges from 300 to 700 nm. The elemental vibration modes of the tests were measured by utilizing Raman spectra of the tests were recorded utilizing BRUKER RFS 27: Stand alone FT-Raman Spectrometer at a determination of 0.2 cm^{-1}. Photoluminescence spectra of the samples were collected at room temperature by using Cary Eclipse (el02045776) Fluorescence spectrophotometer in the wavelength range of 400–800 nm with a Xe laser as an exciting source, and excitation wavelength of 330 nm. The specific surface areas and porous nature of materials were further

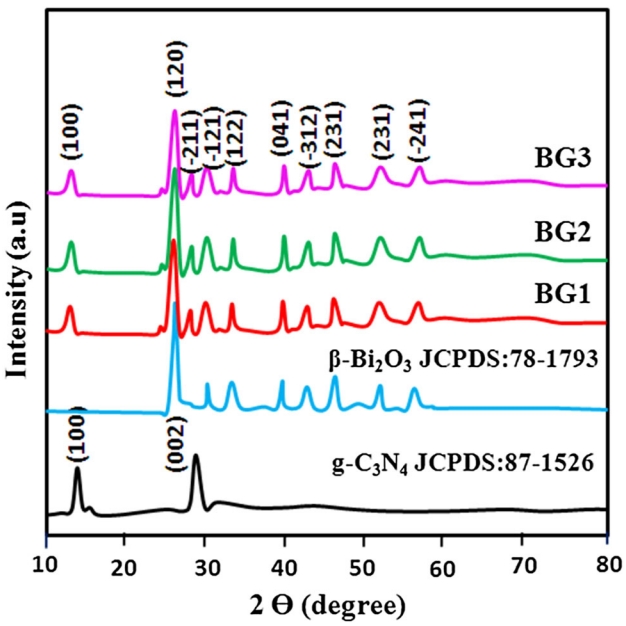

Fig. 1 Powder X-ray diffraction pattern of **a** g-C_3N_4; **b** β-Bi_2O_3 and **c** various β-Bi_2O_3/g-C_3N_4 nanocomposites

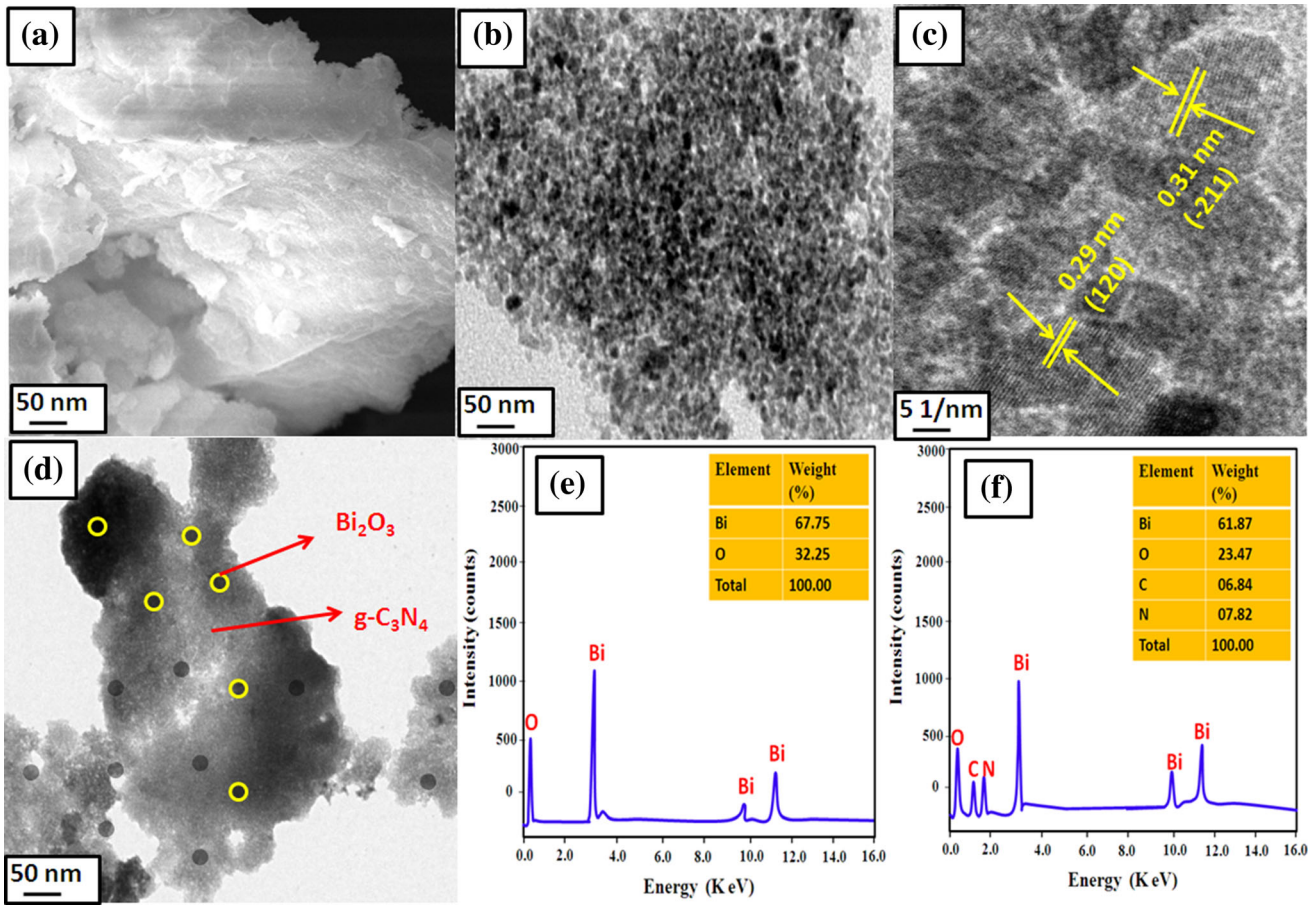

Fig. 2 TEM images of **a** g-C_3N_4, **b**, **c** TEM and HRTEM images of β-Bi_2O_3; **d** TEM image of β-Bi_2O_3/g-C_3N_4; **e**, **f** EDS graph of bare β-Bi_2O_3 and β-Bi_2O_3/g-C_3N_4 (BG3)

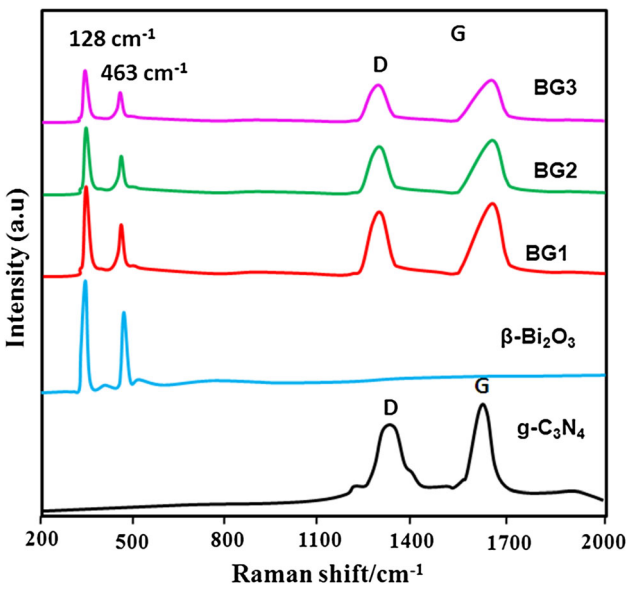

Fig. 3 Raman spectra of pure g-C_3N_4, β-Bi_2O_3 and various β-Bi_2O_3/g-C_3N_4 nanocomposites

investigated by nitrogen adsorption/desorption measurements on nova 2200e.

Photocatalytic Activity Set Up

Within the photocatalytic set up, A 500 W Xenon light with a greatest outflow at around 470 nm was utilized as visible light source. The photocatalytic reactor comprises of a extraordinarily planned quartz glass barrel (30 cm width and 40 cm height). In a typical photocatalytic test, 50 mg of the photocatalyst powder was dissolved in 100 mL of CR and MG fluid solution (5 mg L^{-1}) in a Pyrex reactor. Earlier to light, the suspension was attractively stirred for 1 h within the dark to reach the absorption–desorption equilibrium between dye and the catalyst powders. The visible light time was changed (0, 20, 40,⋯, 100 min) with a customary interval of 20 min. The CR and MG concentration was decided from the absorbance at wavelengths of 500 and 610 nm, separately. The UV–Vis–NIR measurement was performed utilizing PerkinElmer lambda 25 spectrophotometer to determine the absorption.

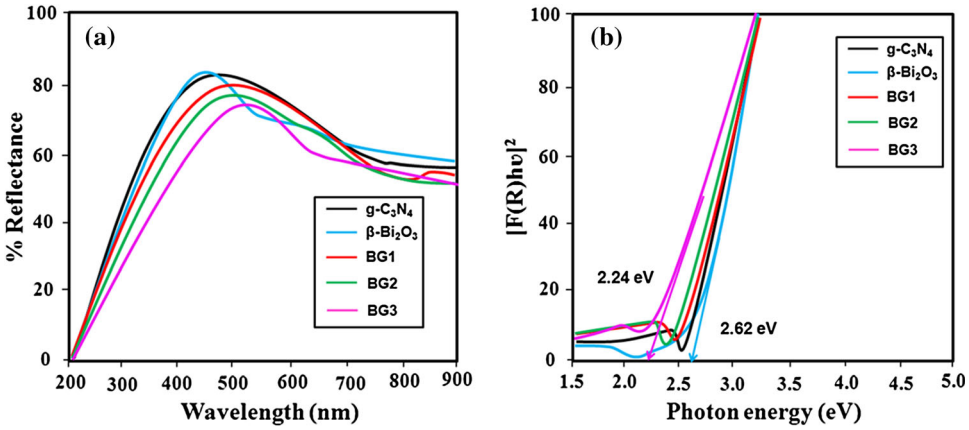

Fig. 4 UV-Vis DRS spectra of the catalysts. **a** Reflectance spectra, **b** Kubelka–Munk model

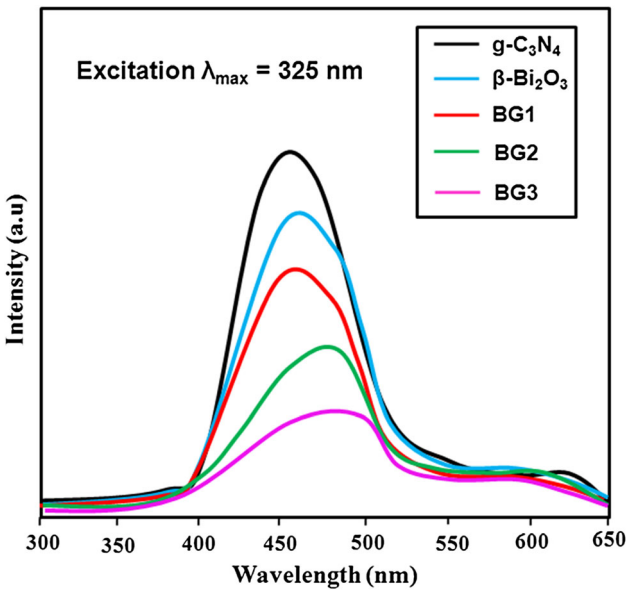

Fig. 5 Photoluminescence spectra of the of the catalyst samples

The degradation of CR and MG was calculated using the ratio of initial (C_0) and final (C) concentration.

Results and Discussion

Figure 1 shows the XRD patterns of as-obtained g-C_3N_4, Bi_2O_3 and Bi_2O_3/g-C_3N_4 composites with different amounts of g-C_3N_4. In bare g-C_3N_4, two typical peaks positioned at 13.11° and 27.49° were indexed to the (100) and (002) crystal plane of g-C_3N_4 [24]. All the diffraction peaks β-Bi_2O_3 could be indexed to tetragonal structure and the finding were agree well with the standard value (JCPDS No. 78-1793) [25]. It is noted that no other impurity phases were detected, and the intensity of the diffraction peaks for β-Bi_2O_3 gradually became wider and less intensity with the increase of g-C_3N_4 content in the Bi_2O_3/g-C_3N_4 composites. The results suggest that decreasing the grain size and it has been confirmed by Scherrer's equation [26]. The average grain size was calculated to be 45, 36, 31, 25 and 20 nm for g-C_3N_4, β-Bi_2O_3, BG1, BG2 and BG3 samples respectively. The surface morphology of the samples was analyzed by using pure g-C_3N_4, β-Bi_2O_3 and various β-Bi_2O_3/g-C_3N_4 samples and the related micrographs were shown in Fig. 2. As shown in Fig. 2a, g-C_3N_4 appeared to be smooth and comprises of nanosheets and randomly aggregated, wrinkled g-C_3N_4 sheets loosely packed together (Fig. 2a). The TEM image of pure β-Bi_2O_3 is clearly visible that individual spherical shaped nanoparticles 35–40 nm with average diameter of around 35–40 nm (Fig. 2b). In order to better recognize the internal structure, the HRTEM image was obtained (Fig. 2c). The clear lattice fringes have a spacing of 0.29 nm and 0.31 nm, respectively, which are assigned to interplanar spacing of (120) and (− 211) of Bi_2O_3, which is also confirmed by XRD results. In β-Bi_2O_3/g-C_3N_4 (BG3) sample, the particles are uniformly distributed on the g-C_3N_4 nanosheets (Fig. 2d). The elemental composition of both pure and sample was identified by using EDS and the associated graph is depicts in Fig. 2e, f. The spectra showed Bi, C, N, O elements, which again proves the heterojunction of and β-Bi_2O_3/g-C_3N_4 composite. Figure 3 shows the Raman spectra of pure g-C_3N_4, β-Bi_2O_3 and β-Bi_2O_3/g-C_3N_4 samples. The Raman spectrum of g-C_3N_4 displays two prominent peaks at 1347 and 1591 cm^{-1}, which correspond to the D and G bands of g-C_3N_4-based materials [27]. In bare β-Bi_2O_3, there are two prominent peaks positioned at 320 and 463 cm^{-1}, which belongs to tetragonal phase of β-Bi_2O_3 [28]. The same band along with D and G band in the β-Bi_2O_3/g-C_3N_4 confirms that formation of heterojunction between β-Bi_2O_3 and g-C_3N_4. Optical absorption and band gap of the catalysts were important factors for measuring its photocatalytic performance. UV-DRS of all the catalysts were measured and the reflectance spectra were shown in Fig. 4a. The optical absorption edge of bare β-Bi_2O_3 was found to be 465 nm, while g-C_3N_4 was identified as

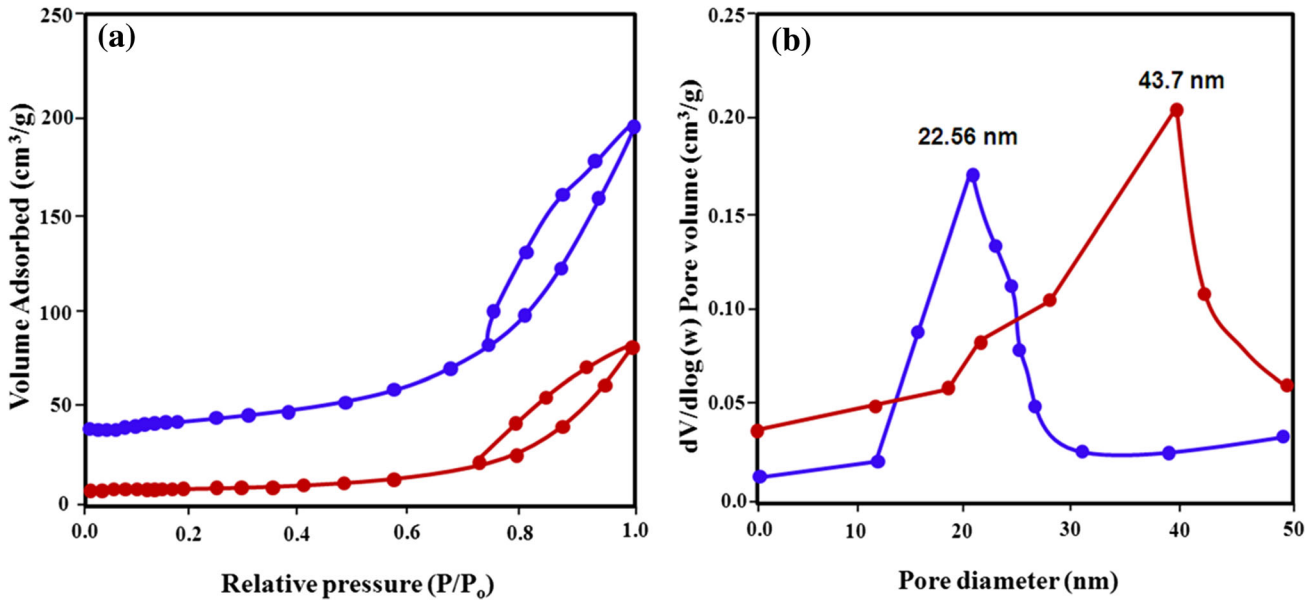

Fig. 6 **a** N_2 adsorption and desorption analysis bare β-Bi_2O_3 and β-Bi_2O_3/g-C_3N_4 (BG3) composite samples, **b** corresponding pore size distribution

480 nm. This absorption edge was further shifted to higher wavelength region with the increases of g-C_3N_4 content. The extended visible light absorption of the β-Bi_2O_3/g-C_3N_4 could absorb more visible light and produced more electron–hole pairs, which results in favorable for improving the photocatalytic performance. Kubelka–Munk (K–M) relation [29] is used to find out the band gap energy of the catalyst. The band gap plot is between $(\alpha h\nu)^2$ vs E_g (Fig. 4b) The intercept straight line was given by corresponding band gap energy of the samples [30, 31]. The band gap energy was established to be 2.62, 2.57, 2.51, 2.40 and 2.25 eV for g-C_3N_4, β-Bi_2O_3, BG1, BG2 and BG3 samples respectively. Room temperature PL spectra were carried for the all the samples with an excitation wavelength of 325 nm using He–Ne laser source and the corresponding graph are shown in Fig. 5. The broad emission peaks were centered at 420–480 nm for all the cases. This main emission can be due to the band–band PL phenomenon [32]. Moreover, the intensity of peak was gradually decreased with the loading of g-C_3N_4. This suggests that suppressed the recombination of photogenerated e–h pairs, which is favorable for enhancing the photocatalytic performance. N_2 absorption–desorption analysis was carried out in order to know the specific surface area and pore size distribution with the results shown in Fig. 6. The spectra showed that both β-Bi_2O_3 and β-Bi_2O_3/g-C_3N_4 (BG3) sample type IV isotherm with H3 hysteresis curve [33], which denotes that mesoporous nature of the samples. The calculated surface area and pore size distribution of BG3 was found to be 103 m^2/g and 22.56 nm respectively. This values is higher than that of bare β-Bi_2O_3 (surface area = 67 m^2/g; pore size = 43.7 nm). The huge surface area could offer the high absorption visible light on its surface of BG3. The photocatalytic activities of the obtained samples were tested by photocatalytic catalytic activity using CR and MG dyes under visible light illuminations. The detailed photocatalytic arrangement set up has been described in our previously published research work [34]. In a typical photocatalytic test, 50 mg of the photocatalyst powder was dissolved in 100 mL of CR and MG fluid solution (5 mg L^{-1}) in a Pyrex reactor. The visible light time was changed (0, 20, 40,⋯, 100 min) with a customary interval of 20 min. The CR and MG concentration was decided from the absorbance at wavelengths of 500 and 610 nm, separately. The UV–Vis–NIR measurement was performed utilizing PerkinElmer lambda 25 spectrophotometer to determine the absorption. The degradation of CR and MG was calculated using the ratio of initial (C_0) and final (C) concentration [35]. UV–Vis absorption spectra of both dyes with were evaluated and the graph is shown in Fig. 7a–d. It was noted that the absorption intensity was gradually decreases with the increase of irradiation time. The intensity was completely disappear after illumination of 100 min visible light. The degradation results over g-C_3N_4, Bi_2O_3, and a series of Bi_2O_3/g-C_3N_4 composites were demonstrated in Fig. 8a, b. Amazingly, all the Bi_2O_3/g-C_3N_4 composites extensively exhibited superior activity in comparison with pure g-C_3N_4 and Bi_2O_3. Especially, the BG3 sample showed the highest activity and 93% of CR in the aqueous solution was degraded within 100 min. This is higher than that of bare g-C_3N_4 (41%) and Bi_2O_3 (45%). The kinetic analysis

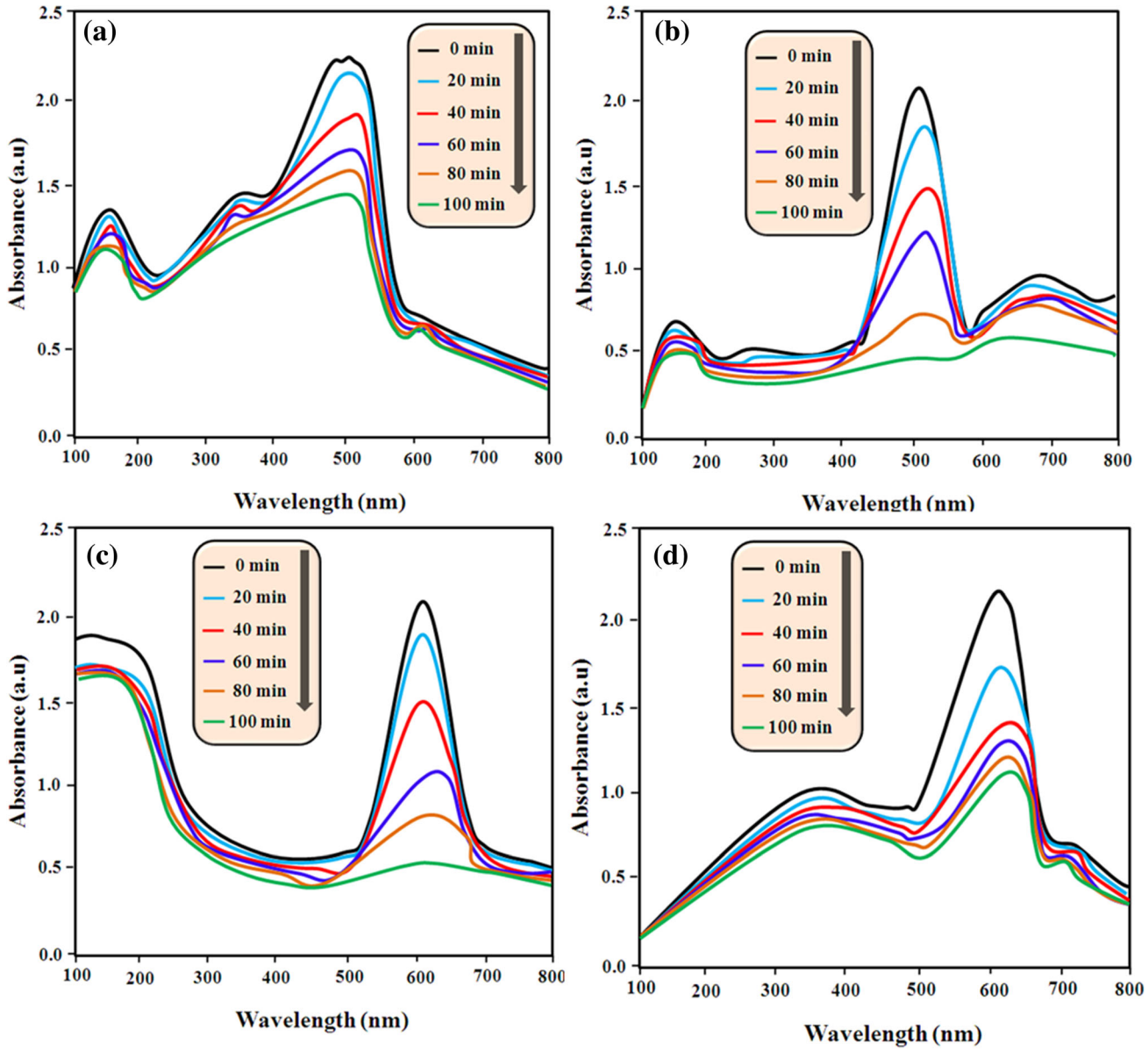

Fig. 7 UV absorption spectra of CR using **a** pure β-Bi_2O_3 and **b** BG3; UV absorption spectra of MG using **c** pure β-Bi_2O_3 and **d** BG3

shows that the photocatalytic reaction can be measured as a first-order reaction (see Fig. 8c, d). The calculated k values for the CR and MG dyes were found to be 0.0398 and 0.0215 min^{-1}, respectively (BG3 sample). This is 15 times higher than that of bare Bi_2O_3 (0.0026 and 0.0014 min^{-1}). The photocatalytic parameters of all the catalysts were shown in Table 1. The stability of photocatalyst is another important role to estimate the photocatalytic efficiency. As can be see form Fig. 9a, b. The photo degradation efficiency of the Bi_2O_3 and Bi_2O_3/g-C_3N_4 (BG3) samples had no considerable decrement after 5 cycling tests (only loss 4.1%), which confirmed that the BG3 sample possessed high stability in catalytic process. The improved photocatalytic performance of Bi_2O_3/g-C_3N_4 composite is due to high surface area and formed p-n junctions between the Bi_2O_3 and g-C_3N_4 NSs. The schematic representation of the possible photocatalytic mechanism is shown in Fig. 9c. When the presence of visible light irradiation, the electrons in their valance bands (VB) could be jumped into their conduction bands (CB) but leaving photo-induced holes in their VB. Nevertheless, distinct the most common composite photocatalysts, the photo-generated electron–hole separation process of Bi_2O_3/g-C_3N_4 composite were to follow Z-scheme. Due to formation of heterojunction between g-C_3N_4 and Bi_2O_3, the electrons on the CB of Bi_2O_3 would rapidly transfer into the VB of g-C_3N_4 to recombine with holes there. As a result, rapidly increases the photogenerated charge carriers as well as reduces their

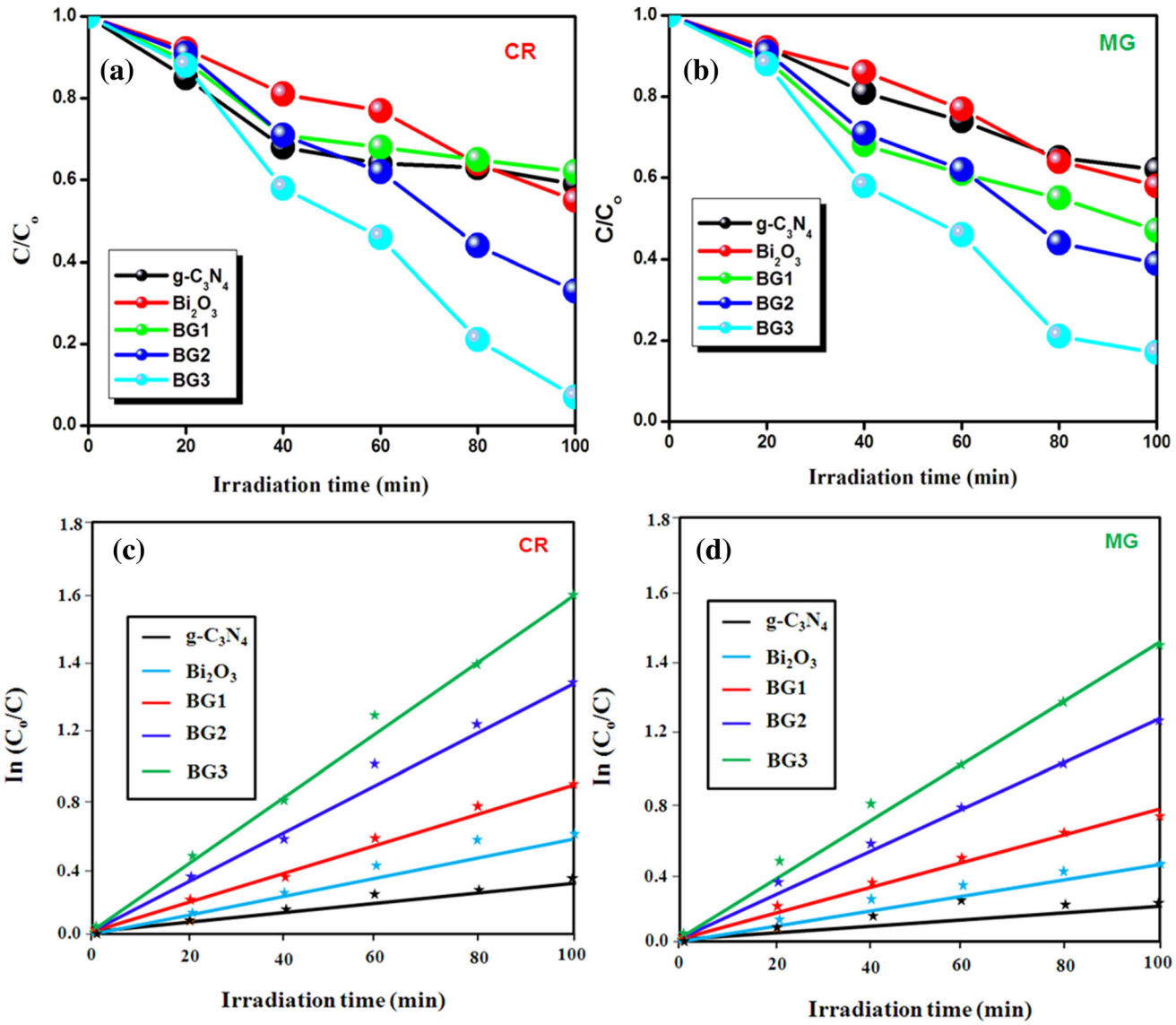

Fig. 8 Temporal degradation profile of **a** CR and **b** MG using pure β-Bi_2O_3 and β-Bi_2O_3/g-C_3N_4 composite samples under visible light; **c** and **d** kinetic fit for the degradation of CR and MG dyes under visible light irradiation

Table 1 Comparison of band gap energy, rate constant and photocatalytic degradation efficiency of pure and β-Bi_2O_3/g-C_3N_4 catalysts

Samples	Band gap (eV)	Rate constant of CR		Rate constant of MG		Degradation efficiency at 100 min	
		K (min^{-1})	R^2	K (min^{-1})	R^2	CR	MG
g-C_3N_4	2.62	0.0026	0.925	0.0014	0.939	41	38
β-Bi_2O_3	2.57	0.0031	0.927	0.0028	0.934	45	42
BG1	2.51	0.0048	0.977	0.0136	0.932	58	53
BG2	2.40	0.0161	0.982	0.0177	0.921	67	61
BG3	2.25	0.0398	0.989	0.0215	0.978	93	83

recombination rate, which results in enhancing the photocatalytic performance. Moreover, ECB of g-C_3N_4 (− 1.12 eV vs. NHE) was more negative than $O_2/{}^*O_2^-$ (− 0.33 eV vs. NHE), the electrons in the CB of g-C_3N_4 would reduce the molecular oxygen to yield $^*O_2^-$ or react with H^+ to form *OH radicals, hence the photocatalytic of

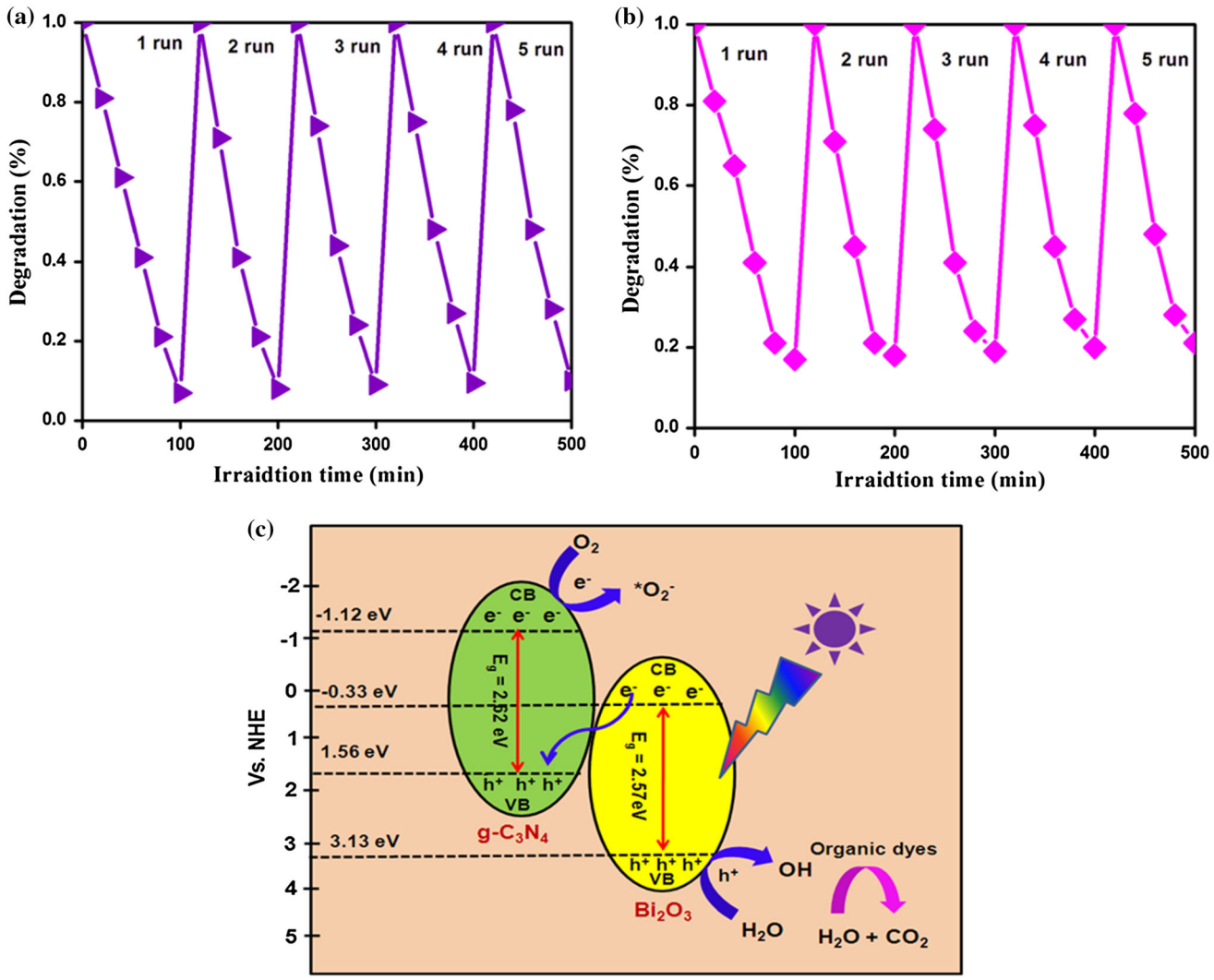

Fig. 9 Recycling test of **a** CR and **b** MG using β-Bi_2O_3/g-C_3N_4 (BG3) catalysts under visible light; **c** photocatalytic mechanism of β-Bi_2O_3/g-C_3N_4 catalysts under visible light irradiation

the Bi_2O_3/g-C_3N_4 system was radically improved. Electrochemical properties were performed in 3 M KOH aqueous electrolyte using a CHI 660E electrochemical workstation. The working electrodes were prepared as follows: 75% Bi_2O_3, 15% conductive carbon black, 10% PTFE (the mass fraction is 10%), and a small amount of ethanol were uniformly mixed. Then the mixture was uniformly coated on a nickel foil with an area of 1 cm^2. Electrochemical impedance spectroscopy (EIS) was performed in a frequency range from 0.01 Hz to 100 kHz. Figure 10a shows the Nyquist plots of the bare Bi_2O_3 and Bi_2O_3/g-C_3N_4 composite samples (BG1 and BG3). The spectra clearly exhibit, semicircle and straight line at the high and low frequencies respectively. Moreover, the spectra represent the solution resistance (Rs), including the intrinsic resistance of active materials, ionic resistance of electrolyte, and contact resistance at the active materials/current collector interface. From Fig. 10a, it can be seen that the values of the sample C Rs and Rct are 0.34 Ω and 0.15 Ω, respectively. This shows that Bi_2O_3/g-C_3N_4 is a low resistance material, which is beneficial to electronic transmission.

Conclusions

In summary, a novel Z-scheme Bi_2O_3/g-C_3N_4 composite photocatalyst has been successfully fabricated via one step microwave irradiation method for the first time. The obtained photocatalyst were methodically studied through XRD, TEM, XPS, BET, UV–vis DRS and PL measurements. The results designated that the g-C_3N_4/Bi_2O_3 composites showed higher photocatalytic activity than that of bare Bi_2O_3 and g-C_3N_4. This could be attributed to the

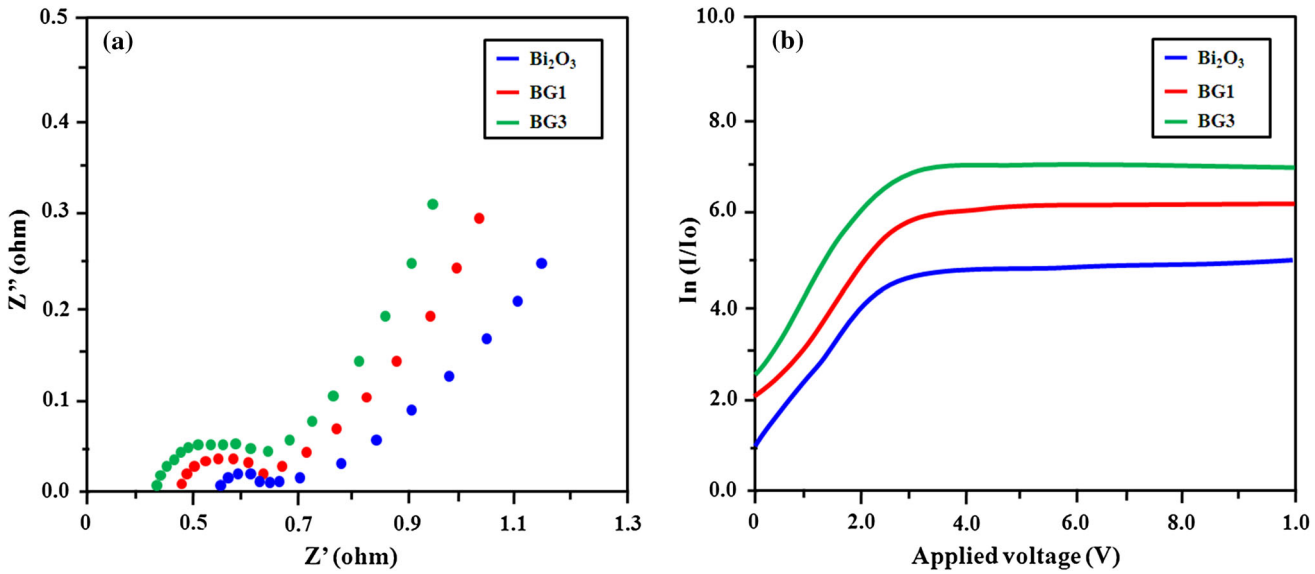

Fig. 10 **a** Nyquist plot of the sample, **b** variance of the value of ln (I/I_O) with the deviation voltage of the prepared samples

appropriate band positions between g-C_3N_4 and Bi_2O_3 and guide to a low recombination between the photogenerated electron–hole pairs. Thus, the results demonstrate that the β-Bi_2O_3/g-C_3N_4 nanocomposites can be used as a promising photocatalyst for removal of antibiotic pollutants.

References

1. K. Breivik, J. M. Armitage, F. Wania, A. J. Sweetman, and K. C. Jones (2016). *Environ. Sci. Technol.* **50**, 798.
2. S. Lee, G. V. Lowry, and H. Hsu-Kim (2016). *Environ. Sci. Process. Impacts* **18**, 176.
3. A. Vengosh, R. Coyte, J. Karr, J. S. Harkness, A. J. Kondash, L. S. Ruhl, R. B. Merola, and G. S. Dywer (2016). *Environ. Sci. Technol. Lett.* **3**, 409.
4. A. Di Paola, E. García-López, G. Marcì, and L. Palmisano (2012). *J. Hazard. Mater.* **211–212**, 3–29.
5. X. Li, J. Yu, and M. Jaroniec (2016). *Chem. Soc. Rev.* **45**, 2603.
6. Y. Choi, M. S. Koo, A. D. Bokare, D. Kim, D. W. Bahnemann, and W. Choi (2017). *Environ. Sci. Technol.* **51**, 3973.
7. G. Fan, Y. Wang, G. Fang, X. Zhu, and D. Zhou (2016). *Environ. Sci. Process. Impacts* **18**, 1140.
8. J. X. Low, J. G. Yu, M. Jaroniec, S. Wageh, and A. A. Al-Ghamdi (2017). *Adv. Mater.* **29**, 1601694.
9. L. L. Sun, G. H. Wang, R. R. Hao, D. Y. Han, and S. Cao (2015). *Appl. Surf. Sci.* **358**, 91.
10. T. M. Di, B. C. Zhu, J. Zhang, B. Cheng, and J. G. Yu (2016). *Appl. Surf. Sci.* **389**, 775.
11. T. M. Di, B. C. Zhu, B. Cheng, J. G. Yu, and J. S. Xu (2017). *J. Catal.* **352**, 532.
12. J. W. Fu, B. C. Zhu, W. You, M. Jaroniec, and J. G. Yu (2018). *Appl. Catal. B: Environ.* **220**, 148.
13. S. V. Prabhakar Vattikuti, Anil Kumar Reddy Police, Jaesool Shim, and Chan Byon (2018). *Appl. Surf. Sci.* **447**, 740.
14. S. V. P. Vattikuti, P. A. K. Reddy, J. Shim, and C. Byon (2018). *ACS Omega* **3**, 7587.
15. E. Serre, E. Rozoy, K. Pedneault, S. Lacour, and L. Bazinet (2016). *Sep. Purif. Technol.* **163**, 228.
16. S. V. P. Vattikuti, B. P. Reddy, C. Byon, and J. Shim (2018). *J. Solid State Chem.* **262**, 106.
17. R. A. He, S. W. Cao, P. Zhou, and J. G. Yu (2014). *Chin. J. Catal.* **35**, 989.
18. G. Liu, S. Li, Y. Y. Lu, J. Zhang, Z. C. Feng, and C. Li (2016). *J. Alloys Compd.* **689**, 787.
19. T. A. Gadhi, A. H. Gordillo, M. Bizarro, P. Jagdale, A. Tagliaferro, and S. E. Rodil (2016). *Ceram. Int.* **42**, 13065.
20. R. A. He, S. W. Cao, and J. G. Yu (2016). *Acta. Phys.-Chim. Sin.* **32**, 2841.
21. X. Xiao, R. Hu, C. Liu, C. Xing, C. Qian, X. Zuo, et al. (2013). *Appl Catal B-Environ.* **140–141**, 433.
22. S. Zuluaga, L. H. Liu, N. Shafiq, S. Rupich, J. F. Veyan, Y. J. Chabal, and T. Thonhauser (2015). *Phys. Chem. Chem. Phys.* **17**, 957.
23. T. Krishnakumar, R. Jayaprakash, M. Parthibavarman, A. R. Phani, V. N. Singh, and B. R. Mehta (2009). *Mater. Lett.* **63**, 896.
24. L. Ge, and C. C. Han (2012). *Appl. Catal. B* **117–118**, 268.
25. X. M. Dang, X. F. Zhang, Y. T. Chen, X. L. Dong, G. W. Wang, C. Ma, X. X. Zhang, H. C. Ma, and M. Xue (2015). *J. Nanopart. Res.* **17**, 93.
26. M. Parthibavarman, K. Vallalperuman, S. Sathishkumar, M. Durairaj, and K. Thavamani (2014). *J. Mater. Sci: Mater. Electron.* **25**, 730.
27. X. Miao, X. Shen, J. Wu, Z. Ji, J. Wang, L. Kong, M. Liu, and Ch Song (2017). *Appl. Catal. A: Gen.* **539**, 104.
28. A. J. Salazar-Pérez, M. A. Camacho-López, R. A. Morales-Luckie, and V. Sánchez-Mendieta (2005). *Superficies y Vacío.* **18**, 4.
29. M. Parthibavarman, V. Hariharan, C. Sekar, and V. N. Singh (2010). *J. Optoelect. Adv. Mater.* **12**, 1894.
30. V. Hariharan, M. Parthibavarman, and C. Sekar (2011). *J. Alloy. Compd.* **509**, 4788.
31. M. Parthibavarman, S. Sathishkumar, and S. Prabhakaran (2018). *J. Mater Sci: Mater. Electron.* **29**, 2341.
32. X. Wang, K. Maeda, A. Thomas, K. Takanabe, G. Xin, J. M. Carlsson, K. Domen, and M. Antonietti (2009). *Nat. Mater.* **8**, 76.

33. D. F. Xu, B. Cheng, S. W. Cao, and J. G. Yu (2015). *Appl. Catal. B: Environ.* **164**, 380.
34. M. Sumathi, A. Prakasam, and P. M. Anbarasan (2019). *J. Mater. Sci: Mater. Electron.* **30**, 3294.
35. M. Parthibavarman, S. Sathishkumar, M. Jayashree, and R. BoopathiRaja (2019). *J. Clust. Sci.* **30**, 351.